

# Carrier Diffusion Lengths Exceeding 1 $\mu\text{m}$ Despite Trap-Limited Transport in Halide Double Perovskites

Milan Delor, Adam H. Slavney, Nathan R. Wolf, Marina R. Filip, Jeffrey B. Neaton, Hemamala I. Karunadasa, and Naomi S. Ginsberg\*



Cite This: *ACS Energy Lett.* 2020, 5, 1337–1345



Read Online

ACCESS |



Metrics & More



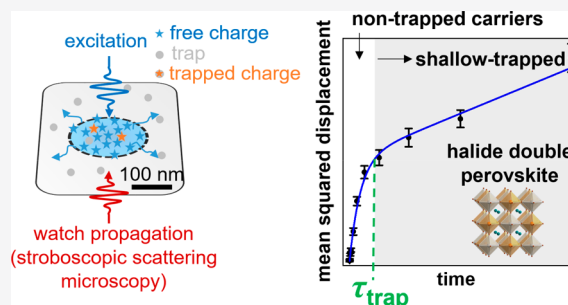
Article Recommendations



Supporting Information

**ABSTRACT:** We image charge carrier transport over nanometers–micrometers and picoseconds–microseconds in halide double perovskites  $\text{Cs}_2\text{AgBiBr}_6$  and  $\text{Cs}_2\text{AgTlBr}_6$  single crystals using stroboscopic scattering microscopy. Both materials exhibit long, microsecond carrier lifetimes because of their indirect or symmetry-forbidden direct bandgaps. We extract free-charge and trap-limited mobilities near the surface and in the crystal bulk. The free-charge mobilities for both materials ( $\sim 10\text{--}50\text{ cm}^2/(\text{V s})$ ) can reach those reported for archetypal lead halide perovskites. We measure trap densities exceeding  $10^{17}\text{ cm}^{-3}$  within  $\sim 20\text{ nm}$  of the crystal surface. Measurements on freshly cleaved or thermally annealed crystals

suggest the traps are primarily halide vacancies that likely form through surface bromine degassing. Although these traps considerably slow charge transport, they are energetically shallow, enabling thermally induced detrapping and mobile carriers over microseconds at room temperature. This defect tolerance yields carrier diffusion lengths exceeding  $1\ \mu\text{m}$  even in the presence of large trap densities and under solar excitation conditions where traps are not saturated. These results suggest that halide double perovskites could rival the best lead-based perovskites for photovoltaic and optoelectronic applications.



Lead-based halide perovskite semiconductors enable conversion efficiencies exceeding 20% in photovoltaic devices despite being processed at low temperatures and from solution, inevitably leading to large material disorder.<sup>1–3</sup> Chemical analogues are needed to both understand the remarkable properties of these materials, as well as to solve issues that currently reduce their commercialization potential, including high toxicity and poor stability. Lead-free double perovskites are emerging as viable candidates to replace archetypal lead halide perovskites because of their high stability, potential for low toxicity, and promising optical properties.<sup>4–15</sup> Here we spatiotemporally visualize carrier dynamics and transport in single crystals of two recently synthesized double perovskites:  $\text{Cs}_2\text{AgBiBr}_6$  and  $\text{Cs}_2\text{AgTlBr}_6$  (Figure 1a), henceforth termed Ag–Bi and Ag–Tl, respectively.<sup>10,11</sup> These materials possess indirect (Ag–Bi) and symmetry-forbidden direct (Ag–Tl) bandgaps, as shown in our density functional theory (DFT) band structure calculations (Figure 1b), as well as in previous reports.<sup>4,6,11,15</sup> While indirect bandgaps require momentum exchange with phonons to enable optical transitions at the band edge, forbidden bandgaps have optical transitions that are disallowed by the inversion symmetry of the electronic states at the band

edge.<sup>16,17</sup> The resulting low optical transition probabilities near the band edges in both indirect and symmetry-forbidden bandgap materials suppress radiative recombination of carriers. Both Ag–Bi and Ag–Tl therefore possess long carrier lifetimes in the microsecond regime.<sup>10–13,15</sup> Despite the weak optical transition probability near the symmetry-forbidden band edge of Ag–Tl, the absorption coefficient rapidly increases to  $\sim 10^5\text{ cm}^{-1}$  a few hundred meV above the band-edge.<sup>11</sup> As such, the symmetry-forbidden bandgap provides an attractive balance of large absorption coefficients and long carrier lifetimes, ideal for solar energy-harvesting applications.

Beyond large absorption coefficients and long carrier lifetimes, long carrier diffusion lengths (and thus large mobilities) are necessary to enable useful extraction of photogenerated carriers. Although carrier mobilities in Ag–

Received: February 22, 2020

Accepted: March 30, 2020

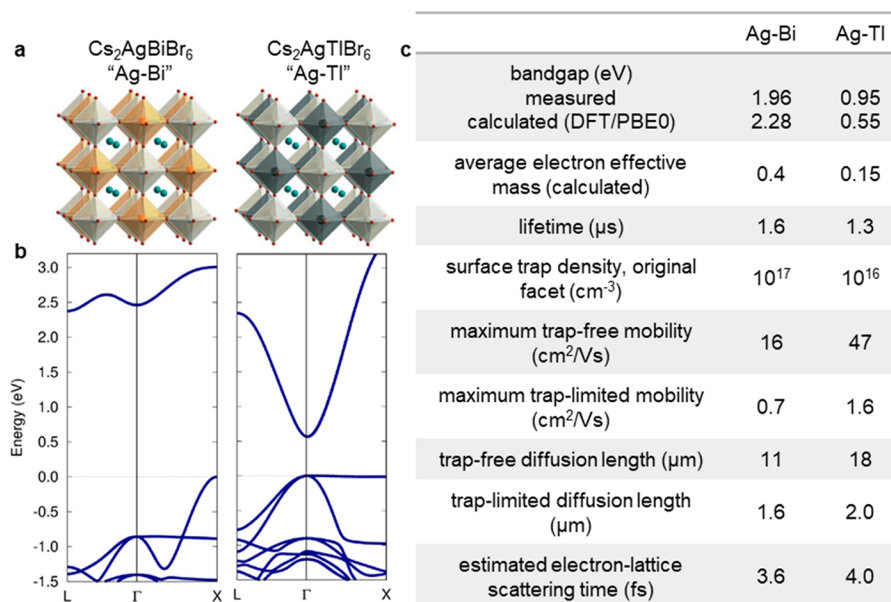


**Figure 1.** (a) Double perovskites  $\text{Cs}_2\text{AgBiBr}_6$  (Ag–Bi) and  $\text{Cs}_2\text{AgTlBr}_6$  (Ag–Tl) with Ag, Bi, Tl, Cs, and Br atoms represented as white, orange, gray, turquoise, and brown spheres, respectively. (b) Band structures of Ag–Bi (left) and Ag–Tl (right) calculated with DFT-PBE0, as described in Materials and Methods in the Supporting Information. (c) Measured and calculated material parameters related to charge transport for Ag–Bi and Ag–Tl. The bandgap values are for the indirect  $X \rightarrow L$  (Ag–Bi) and symmetry-forbidden  $\Gamma \rightarrow \Gamma$  (Ag–Tl) transitions. The electron effective mass is calculated as the isotropic average of the inverse second derivatives of the conduction band with respect to the crystal momentum around the L- (Ag–Bi) and  $\Gamma$ - (Ag–Tl) points, as described in the Materials and Methods in the Supporting Information. The reported mobilities are for cleaved Ag–Bi single crystals and unannealed Ag–Tl single crystals. See text for details of all other parameters extracted from stroboSCAT measurements.

Tl have never been characterized, Ag–Bi was investigated using space charge limited current<sup>7</sup> and time-resolved microwave conductance (TRMC),<sup>18,19</sup> with reported mobilities ranging between 1 and  $12 \text{ cm}^2/(\text{V s})$ . These methods are either spatiotemporally or spatially averaged measures of carrier mobilities; while powerful, they can neither disentangle surface versus bulk effects, nor directly characterize temporal heterogeneity in carrier mobilities without prior assumptions. Surfaces dictate efficiencies in devices requiring surface charge extraction,<sup>20</sup> like in traditional photovoltaic architectures. To investigate the fundamental properties of double perovskites and their promise for future photovoltaic or optoelectronic applications, we therefore need methods capable of moving beyond spatiotemporally averaged figures of merits to characterize near-surface versus bulk material properties, including defect densities, and the relationship between these spatially inhomogeneous properties and charge carrier dynamics. In this study, we use stroboscopic scattering microscopy (stroboSCAT),<sup>21</sup> a recently developed tool that directly images carrier transport with high spatiotemporal resolution, to characterize carrier mobilities, lifetimes, diffusion lengths, defect densities, and the role of these defects near the surfaces of Ag–Bi and Ag–Tl single crystals. The main parameters extracted from our measurements and DFT calculations are summarized in Figure 1c. Below, we first describe how stroboSCAT enables extracting these parameters and then discuss results for Ag–Bi and Ag–Tl single crystals. We find that trap densities near the crystal surfaces (likely halide vacancies) are very high, but the traps are shallow enough to enable defect tolerance over the full carrier lifetimes, resulting in carrier diffusion lengths exceeding  $1 \mu\text{m}$  even in the presence of such large trap densities. Despite these already advantageous properties, we show that trap densities and

carrier–lattice interactions can be substantially modified through crystal cleaving and annealing, suggesting that carrier–defect interactions can be readily manipulated in double perovskites to enhance their functional properties.

stroboSCAT is a time-resolved optical microscopy approach that measures carrier-induced changes to light backscattering (Figure S1).<sup>21</sup> First, a nearly diffraction-limited pump pulse (300 nm full-width at half-maximum, fwhm) excites electrons into the conduction band of the semiconductor; a time-delayed widefield probe then images how the optical scattering profile of the material changes in response to pump excitation. The probe is detected on a camera in a reflection geometry, with its frequency detuned from the band-edge of the material. The probe primarily senses pump-induced changes to the real part of the material's refractive index. Because charge carriers modify the material's local electric polarizability, the spatial distribution of carriers and its evolution as a function of time are directly imaged by the probe. The expansion of the carrier distribution reports on the mean squared displacement,  $\text{m.s.d.} = \sigma^2(t) - \sigma^2(0) = 2Dt$ , where  $\sigma^2(t)$  is the variance of the Gaussian function describing the spatial distribution of the carriers at time  $t$ .  $D$  is the carrier diffusivity, related to the mobility through the Einstein relation. The spatial sensitivity to carrier motion is dictated by the signal-to-noise ratio rather than the diffraction limit; for this study, a precision of  $\Delta\sqrt{2Dt} \approx 15 \text{ nm}$  is obtained. We note here that we do not currently have the ability to distinguish electron versus hole contributions to the stroboSCAT contrast and therefore observe an average of the two contributions. Ag–Bi under current growth conditions is thought to be slightly p-type, and Ag–Tl is thought to be slightly n-type;<sup>7,11</sup> nevertheless, because in both cases the estimated equilibrium excess carrier densities ( $<10^{15} \text{ cm}^{-3}$ ) are much lower than the initial

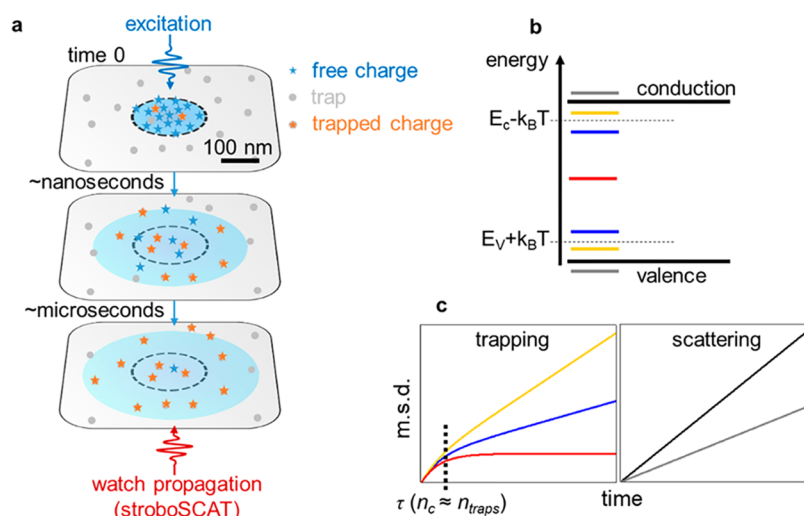


**Figure 2.** Spatiotemporally resolved trapping and scattering using stroboSCAT. (a) Localized excitation creates a concentration gradient of free charges ( $n_c$ , blue stars) with a known peak concentration at time zero, which may be larger than the trap density ( $n_{\text{traps}}$ , gray dots), so that most carriers experience a trap-saturated regime. The charges then diffuse out of the initial excitation volume, eventually reducing the free charge concentration to below the trap density, thus crossing into a regime in which all carriers can be trapped (orange stars). (b) Schematic energy-level diagram of a semiconductor with defects at different energy levels and (c) their expected effects on the measured mean squared displacement (m.s.d.) of charges in stroboSCAT experiments. The different behaviors are color-coded with respect to defect types labeled in (b).  $\tau (n_c \approx n_{\text{traps}})$  corresponds to the time at which the carrier density approaches the trap density in the material. For deep traps (red), the m.s.d. turns over and eventually stagnates when all carriers are trapped. For shallow traps (blue and gold), the m.s.d. turns over but keeps increasing throughout the lifetime of carriers, with a slope determined by the energy difference between the trap and the conduction/valence band. For above-gap defects, the m.s.d. remains linear (diffusive) but the slope decreases compared to the defect-free behavior (gray line compared to black line) as carrier–defect interactions increase.

photoinduced carrier densities in this study ( $>10^{17} \text{ cm}^{-3}$ ), our results are representative of ambipolar carrier transport in intrinsic (undoped) Ag–Bi and Ag–Tl.

Although closely related to other spatiotemporally resolved microscopies<sup>22,23</sup> such as transient absorption microscopy<sup>24–26</sup> and transient photoluminescence microscopy,<sup>27,28</sup> stroboSCAT and related transient reflection microscopies<sup>21,29,30</sup> are mostly sensitive to processes occurring within  $\sim 10$ – $20 \text{ nm}$  of the crystal surface (with a tunable penetration depth depending on probe wavelength and material absorption), thus primarily reporting on near-surface rather than entirely bulk dynamics. A reflection rather than transmission geometry also enables probing thick and opaque materials such as the millimeter-scale single crystals studied here. Using stroboSCAT, we resolve charge carrier motion over nine spatiotemporal orders of magnitude. Access to such multiscale characterization is, as will be shown, necessary for these materials that display spatiotemporally inhomogeneous dynamics because of carrier–defect interactions.

In stroboSCAT and related spatiotemporally resolved microscopies, tracking carrier diffusion out of an initially diffraction-limited excitation spot has an important consequence: the carrier density reduces substantially over time because of both carrier recombination and diffusion. Thus, density-dependent processes such as carrier trapping, carrier–carrier scattering, and Auger recombination display time-dependent behavior. Of particular importance to this study is that the density of unfilled trap sites evolves over time (Figure 2a): at early times, the free carrier density can substantially exceed the trap density, so that all traps are rapidly filled and the majority of carriers sense a trap-saturated landscape.<sup>31</sup> As the density of carriers drops to below the trap density, the number of unfilled traps increases, thus increasing the proportion of trapped versus untrapped carriers. Defects can

either lie deep within the bandgap (Figure 2b, red, deep traps), within a few  $kT$  of the conduction or valence bands (blue, gold, shallow traps), or within the conduction/valence bands (gray), at which point they act only as scattering sites. Each of these defect types influences the mean squared expansion of the photogenerated carrier distribution observed in stroboSCAT in a distinct way, either reducing or entirely stopping it, as illustrated in Figure 2c. Here we exploit the defect dependence of the time-dependent mean squared expansion to characterize the density and type of near-surface defects in double perovskites.

We begin by describing results on the archetypal double perovskite Ag–Bi to benchmark our stroboSCAT measurements of carrier lifetimes and mobilities against previous reports. TRMC and SCLC measurements show mobilities in the range of  $1 < \mu < 12 \text{ cm}^2/(\text{V s})$ ,<sup>7,18</sup> while lifetimes measured from photoluminescence and transient absorption range from  $600 \text{ ns} < \tau < 1.4 \mu\text{s}$ .<sup>10,12</sup> Taken together, these numbers would imply a charge carrier diffusion length of  $1.7 \mu\text{m} < L_d < 10 \mu\text{m}$ , assuming carriers retain the reported mobilities throughout their lifetimes. Our stroboSCAT measurements concur with previous photoluminescence lifetime measurements, showing a rapid decay on the few-nanosecond time scale of  $\sim 30\%$  of the photogenerated carrier population, followed by a slow  $\sim 1.6 \mu\text{s}$  lifetime for  $\sim 70\%$  of the carrier population (Figure S2).<sup>10,12,13,32</sup> The measured average carrier diffusivities (and hence mobilities,  $\mu$ ), however, are not temporally uniform over the lifetime of the carriers. Figure 3b displays a representative mean squared displacement curve, showing a turnover from an initial, fast diffusivity of  $0.16 \text{ cm}^2/\text{s}$  ( $\mu = 6 \text{ cm}^2/(\text{V s})$ ) to a slower diffusivity of  $0.007 \text{ cm}^2/\text{s}$  ( $\mu = 0.27 \text{ cm}^2/(\text{V s})$ ) beyond  $30 \text{ ns}$  delay between pump and probe pulses. Fast initial diffusivity could be due either to nonlinear recombination processes (e.g., Auger recombination) being larger at the

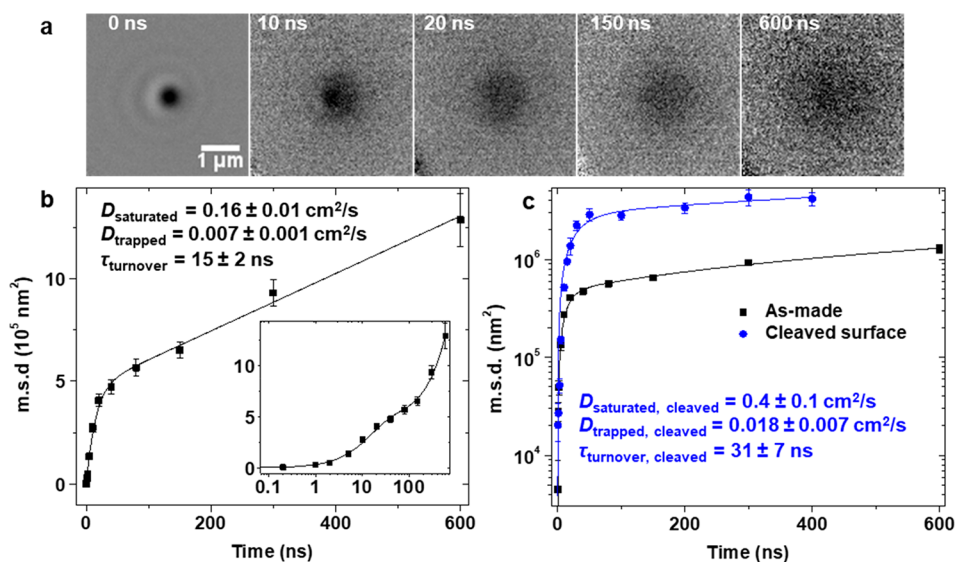


**Figure 3.** Carrier diffusion in Ag–Bi. (a) Representative stroboSCAT time series on a Cs<sub>2</sub>AgBiBr<sub>6</sub> single crystal. The pump is tuned to 440 nm with an initial carrier density of  $4 \times 10^{18} \text{ cm}^{-3}$ . The probe is tuned to 640 nm. Data at other excitation wavelengths are provided in Figures S5 and S6. (b) Mean squared displacement (m.s.d.) for the data shown in panel a, obtained through Gaussian fits to the expanding carrier distribution. Error bars are standard deviations derived from Gaussian fitting. The m.s.d. is nonlinear, exhibiting a turnover from high to low diffusivity. We assign early time behavior to trap-saturated charge diffusivity in this material, and late-time behavior to an effective diffusivity for charges being trapped and thermally detrapped from shallow trap states (corresponding to blue or gold scenarios in Figures 2b,c). The solid curve is a fit using an exponentially decaying diffusivity from  $D_{\text{saturated}}$  to  $D_{\text{trapped}}$  with a turnover time  $\tau$ . The semilog scale inset displays the high fit quality over 4 orders of magnitude in time. (c) Comparison of m.s.d. for the original crystal (black, same data as in panel b) to m.s.d. for a freshly cleaved crystal (blue). Note the log scale.  $D_{\text{saturated}}$  and  $D_{\text{trapped}}$  are both  $\sim 2.5$  times larger in the freshly cleaved crystal data, indicating lower lattice scattering compared to the as-made crystal; the turnover time is also twice as large, indicating less trapping near the cleaved surface.

center of the excitation profile,<sup>25,28</sup> where the carrier density is largest, or to a change in carrier diffusivity. We rule out nonlinear recombination through power-dependent measurements that monitor the total carrier population decay in the first few nanoseconds (largest carrier density) over pump excitation fluences ranging from 35 to 115  $\mu\text{J}/\text{cm}^2$  (Figure S3). The results show no nonlinearities over this range of fluences, in accordance with previous measurements using ensemble transient absorption,<sup>12</sup> though nonlinear dynamics were observed at lower fluences in polycrystalline thin films,<sup>18,19</sup> where the grain boundaries may prevent carrier density from decreasing as readily as in a single crystal over the nanosecond duration of the excitation. In the measurements shown in Figure 3, we use a fluence of 66  $\mu\text{J}/\text{cm}^2$  using 100 ps pulse-width laser diodes, corresponding to a peak carrier density of  $4 \times 10^{18} \text{ cm}^{-3}$ . We show below that the desaturation of shallow traps is likely responsible for the observed turnover in the transport regime.

Previous temperature-dependent TRMC measurements<sup>18,19</sup> in Ag–Bi identified shallow trapping as a key process in these materials. Thermal fluctuations enable carriers in shallow traps to detrapp with a probability dictated by Boltzmann statistics. As such, free carriers remain mobile throughout their lifetimes. However, the measurements did not directly quantify the effect of shallow trapping on charge mobility and overall diffusion lengths. On the basis of these temperature-dependent TRMC studies and the fact that our early time diffusivities correspond closely to those reported in the literature using both SCLC<sup>7</sup> and TRMC,<sup>18</sup> we assign the fast-to-slow transition observed in stroboSCAT measurements to a trap saturation effect (Figure 2). At early times, all traps are filled, and the observed diffusivity corresponds to the charge diffusivity of free,

untrapped carriers in a lattice whose shallow traps are saturated ( $D_{\text{saturated}}$ ). Past  $\tau_{\text{turnover}}$  traps become unsaturated and the observed behavior provides an effective diffusivity for shallowly trapped charges that remain partially mobile because of occasional thermal detrapping ( $D_{\text{trapped}}$ ). A 23-fold lower  $D_{\text{trapped}}$  compared to  $D_{\text{saturated}}$  implies a 23:1 ratio of trapped to untrapped carriers once the carrier density has dropped below the trap density. A Boltzmann ratio of 23 at room temperature implies that traps have energies on the order of  $\sim 80 \text{ meV}$  below (above) the conduction (valence) bands, i.e. of  $\sim 3 \text{ kT}$ .

We fit the m.s.d. to a phenomenological model that assumes an exponentially decaying saturated-trap diffusivity succumbing to a “baseline” effective diffusivity for trapped charges, i.e.  $D = (D_{\text{saturated}} - D_{\text{trapped}})e^{-t/\tau_{\text{turnover}}} + D_{\text{trapped}}$ , which leads to an m.s.d. that can be fit with  $2\tau_{\text{turnover}}(D_{\text{saturated}} - D_{\text{trapped}}) \times (1 - e^{-t/\tau_{\text{turnover}}}) + 2D_{\text{trapped}}t$ .<sup>33</sup> The fit quality and extracted parameters are shown in Figure 3b. Although empirical, the model provides an intuitive picture of carrier transport behavior. Beyond the saturated-trap and shallow-trapped carrier diffusivities, we extract a characteristic  $\tau_{\text{turnover}}$  time that enables extracting the approximate trap density near the crystal surface. At  $\tau_{\text{turnover}} = 15 \text{ ns}$ , accounting for carrier diffusion and recombination, the carrier density has dropped by a factor of 18 compared to its  $t = 0$  value of  $4 \times 10^{18} \text{ cm}^{-3}$ , suggesting that the shallow trap density is  $\sim 2 \times 10^{17} \text{ cm}^{-3}$ . As will be seen below, the mobilities in the crystal bulk are larger than near the surface, so that when accounting for three-dimensional carrier diffusion, the carrier density at 15 ns (and thus the trap density) may be closer to  $\sim 1 \times 10^{17} \text{ cm}^{-3}$  (see methods in the Supporting Information). This number is an order of magnitude greater than the trap density estimated from bulk TRMC measurements of Ag–Bi single crystals ( $10^{16}$

$\text{cm}^{-3}$ ),<sup>18</sup> suggesting that trap densities are  $\sim 10$  times larger near the surface than in the crystal bulk. Fluence-dependent m.s.d. traces recorded with excitation densities down to  $10^{17} \text{ cm}^{-3}$  are shown in Figure S4, showing that the m.s.d. approaches linear (diffusive) behavior with  $D \approx D_{\text{trapped}}$  as the initial photoinduced carrier density is lowered below the trap density. These results lend support to our hypothesis that the turnover in the m.s.d. is indeed due to a trap-saturation effect at early times.

With reasonable signal-to-noise ratio, we are able to follow carrier dynamics down to a carrier density of  $\sim 10^{15} \text{ cm}^{-3}$  at late times. In this late time regime there is no evidence of deep trapping, which would halt diffusion and lead to a flat m.s.d. versus time (red trace in Figure 2). This result thus provides an upper bound of  $\sim 10^{15} \text{ cm}^{-3}$  for the deep trap density near the surface of these materials. Under the excitation conditions used, the ambipolar diffusion length of photogenerated electrons and holes in  $\text{Cs}_2\text{AgBiBr}_6$  as measured by stroboSCAT is  $\sqrt{2D_{\text{saturated}}\tau_{\text{turnover}} + 2D_{\text{trapped}}(\tau - \tau_{\text{turnover}})} = 1.6 \mu\text{m}$ . Under typical steady-state operating conditions with solar irradiation, the traps would not be saturated. The carrier diffusion length would then still reach  $\sim 1.4 \mu\text{m}$  because of long lifetimes and the predominance of shallow over deep trapping (see the Supporting Information for more detail).

To further test our hypothesis regarding the two transport regimes observed in stroboSCAT, we measure carrier transport near a freshly cleaved crystal surface. A freshly cleaved surface typically exhibits lower impurity concentrations, heterogeneities, and trap densities, owing primarily to briefer atmospheric and solvent exposure.<sup>34</sup> Spontaneous halogen degassing from the crystal surface and finite halide vacancy diffusivities may also give rise to larger vacancy densities near an original crystal facet than at a freshly cleaved facet that has not had time to fully equilibrate with its surroundings. To ensure the cleaved surface is as representative of the bulk as possible, we cleave the crystal in a nitrogen glovebox with  $< 1$  ppm of  $\text{O}_2$  and  $\text{H}_2\text{O}$ , place the cleaved surface on an optical substrate, immediately drop-cast a solution of PMMA on top of it, and perform stroboSCAT measurements within 3 h of cleaving. A comparison of the measured m.s.d. under the same excitation conditions for cleaved versus as-made crystals is shown in Figure 3. A similar dual transport regime is observed in the cleaved crystals. With lower shallow-trap densities, one would expect a longer turnover time but unchanged early time diffusivities. We indeed observe a longer turnover time of 31 ns, implying a shallow trap density of  $(3-4) \times 10^{16} \text{ cm}^{-3}$  after accounting for carrier recombination and three-dimensional bulk diffusion. This number is closer to that estimated for the bulk of Ag–Bi single crystals from TRMC measurements,<sup>18</sup> suggesting the freshly cleaved surface is indeed more representative of the bulk than the original surface. The longer turnover time (lower trap density) is to be expected for the freshly cleaved surface. An unexpected observation, however, is the larger diffusivities at both early and late times, indicating lower carrier–lattice scattering (Figure 2, gray and black traces) near the cleaved compared to the original surface. With the measured diffusivities of  $D_{\text{saturated}} = 0.4 \text{ cm}^2/\text{s}$  ( $\mu = 16 \text{ cm}^2/(\text{V s})$ ) and  $D_{\text{trapped}} = 0.018 \text{ cm}^2/\text{s}$  ( $\mu = 0.7 \text{ cm}^2/(\text{V s})$ ) near the cleaved surface, the diffusion length under current experimental conditions is  $2.4 \mu\text{m}$ . Under solar fluences (unfilled traps), the diffusion length would be  $1.6 \mu\text{m}$ . Should traps be passivated to operate in a fully trap-saturated regime at solar

fluences, the diffusion length would be  $11 \mu\text{m}$ . Such large diffusion lengths, even in the trap-limited regime, make these materials promising for a range of electronic devices.

The observed changes in  $D_{\text{saturated}}$  and  $D_{\text{trapped}}$  near the cleaved versus original surface provide an interesting opportunity to study carrier–lattice interactions. Carrier–lattice scattering occurs primarily through carrier–phonon or carrier–charged defect scattering,<sup>35</sup> which are distinct processes from carrier trapping. Although lower carrier scattering at the cleaved surface is phenomenologically different from the lower trapping probability, these effects may be mechanistically related, as described below. Halide vacancies are prime contenders for shallow trapping in halide perovskites; their formation enthalpies are relatively low, and they typically form shallow traps within a few kT of the conduction band.<sup>36–40</sup> Degassing of  $\text{Br}_2$  was also observed with mass spectrometry in a related double perovskite (Ag–Tl).<sup>11</sup> We therefore assign the observed shallow trapping primarily to halide vacancies that form spontaneously through halogen degassing from the surface, leading to a lower vacancy concentration in the bulk than near the surface. The lower vacancy concentration at the cleaved surface is expected to increase both  $\tau_{\text{turnover}}$ , because of slower trap desaturation, and  $D_{\text{trapped}}$  because of lower carrier–trap encounter in the unsaturated regime. The observed increase of  $D_{\text{saturated}}$ , however, cannot be readily explained through a change in shallow trapping probability. Instead, it must be due to lower carrier–lattice scattering near the freshly cleaved surface. Assuming the  $2.5\times$  increase in  $D_{\text{trapped}}$  is fully accounted for by a lower carrier–unfilled trap encounter rate, the concomitant  $2.5\times$  increase in  $D_{\text{saturated}}$  must be explained by a mechanism affecting only the early time trap-saturated regime. As such, we hypothesize that filled traps increase carrier scattering, either through neutral defect scattering or through increased lattice disorder.<sup>41,42</sup> Indeed, filled traps can significantly distort the local lattice,<sup>43</sup> introducing disorder that likely leads to greater carrier–lattice scattering. Thus, with decreased shallow trap densities near the cleaved surface, the early time encounter rate of free charges with filled traps is decreased; similarly, the encounter rate of free charges with unfilled traps is decreased at late times by an equivalent factor, explaining the concomitant increase of  $D_{\text{saturated}}$  and  $D_{\text{trapped}}$  near the cleaved surface. Future direct identification of the nature of defects in these materials, and theoretical treatments of the effect of filled traps on polaronic transport, will be needed to confirm our hypothesis.

Although Ag–Bi shows promising diffusive properties, its relatively large and indirect bandgap within the visible region would negatively affect its ability to harvest a significant fraction of solar photons for photovoltaic applications. Recently, an exceptionally low direct but symmetry-forbidden bandgap of 0.95 eV was achieved through Tl substitution for Bi,<sup>11</sup> heavily perturbing the material band structure (Figure 1) and enabling appreciable absorptivity across the visible spectrum of  $(4-5) \times 10^4 \text{ cm}^{-1}$ . The lack of photoluminescence and the low bandgap in this material complicate lifetime and mobility characterization with traditional approaches. stroboSCAT's reliance on nonresonant back-scattering, however, helps to circumvent these difficulties. The carrier lifetimes in as-made single crystals of Ag–Tl are similar to Ag–Bi: we measure the major (68%) lifetime component as  $1.3 \mu\text{s}$  (Figure S7), corroborating TRMC lifetime measurements.<sup>11</sup> The carrier m.s.d. (Figure 4) for Ag–

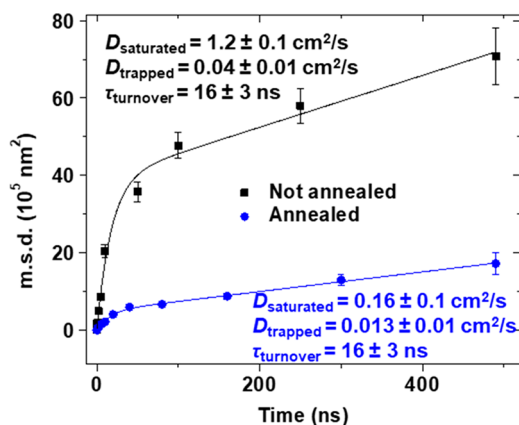


Figure 4. Carrier diffusion in Ag–Tl. m.s.d. extracted from stroboSCAT measurements for the same crystal of  $\text{Cs}_2\text{AgTlBr}_6$  before and after annealing on a hot plate in a nitrogen glovebox at 100 °C for 4 days. The solid curves are fits using the same exponentially decaying diffusivity model as that used for Ag–Bi.

Tl looks qualitatively similar to that for Ag–Bi, with a fast transport regime followed by a slower one. We thus use the same model to fit and interpret the data. In as-made (uncleaved, unannealed) crystals, the fast transport regime has  $D_{\text{saturated}} = 1.2 \text{ cm}^2/\text{s}$  ( $\mu = 47 \text{ cm}^2/(\text{V s})$ ), which is as high as for single crystals of archetypal methylammonium lead iodide and bromide perovskites.<sup>44</sup> Shallow trapping results in  $D_{\text{trapped}} = 0.04 \text{ cm}^2/\text{s}$  ( $\mu = 1.6 \text{ cm}^2/(\text{V s})$ ) at late times. The turnover time of 16 ns suggests a near-surface shallow trap density of  $\sim 10^{16} \text{ cm}^{-3}$ , comparable to the cleaved surface of Ag–Bi. The 30:1 ratio in early versus late time diffusivities implies a shallow trap lying 87 meV below (above) the conduction (valence) band, again similar to Ag–Bi. The 3× faster transport in as-made Ag–Tl compared to cleaved Ag–Bi is quantitatively consistent with the calculated electron effective masses (Figure 1b,c), and with the expected linear relationship between bandgap and effective mass. The measured diffusivities and calculated effective masses can be used to estimate carrier–lattice scattering times of  $\sim 4 \text{ fs}$  for both materials, remarkably similar to that measured in methylammonium lead iodide perovskites at room temperature<sup>45</sup> and implying similarly strong electron–phonon coupling in these double perovskites.

Thermal annealing of Ag–Tl is known to promote bromide loss as  $\text{Br}_2$  vapor from the crystal surface, resulting in two cationic halide vacancies and two electrons donated to the material for each  $\text{Br}_2$  molecule that leaves the material.<sup>11</sup> This process allows measuring the effect of a specific type of defect—the halide vacancy—and further testing of our hypotheses on carrier–defect interactions in double perovskites. In Ag–Tl crystals annealed on a hot plate in a nitrogen glovebox at 100 °C for 4 days, stroboSCAT shows  $D_{\text{saturated}}$  and  $D_{\text{trapped}}$  are reduced by factors of 8 and 3, respectively (Figure 4). The turnover time is not affected by annealing, but we put forth that this congruence is a misleading coincidence: accounting for the much slower carrier diffusion, a turnover time of 16 ns in annealed crystals implies a near-surface shallow trap density of  $\sim 2.5 \times 10^{17} \text{ cm}^{-3}$ , a 25-fold increase in shallow trap density induced by annealing. These results lend support to the hypothesis advanced for Ag–Bi that halide vacancies are responsible for both shallow trapping (when unfilled) and carrier–lattice scattering (when filled). Never-

theless, the inequivalent respective  $\sim 8$ -fold and  $\sim 3$ -fold decreases in the fast (early) and slow (late) transport regimes indicate that multiple factors contribute to the reduced mobilities in annealed Ag–Tl crystals. Indeed, annealing may reduce the densities of other types of traps.<sup>7</sup> A reduction in trap sites other than halide vacancies, in combination with an increase in halide vacancies, would indeed cause a more modest reduction in  $D_{\text{trapped}}$  than  $D_{\text{saturated}}$ , as observed. Thus, although halide vacancies appear to dominate carrier–defect and affect carrier–lattice interactions in double perovskites, the defect chemistry in these materials is likely complex, with defect–lattice, defect–carrier, and defect–defect interactions all contributing to the local electronic and phononic band dispersions.

Overall, the calculated total diffusion length over the full carrier lifetimes of 1.3  $\mu\text{s}$  under current experimental conditions for unannealed Ag–Tl crystals approaches an impressive 4  $\mu\text{m}$ . At solar fluences, for which traps would not be saturated to the extent that they are in our present measurements, the diffusion length would be 2  $\mu\text{m}$ . In a scenario in which all traps are saturated (trap density  $< 10^{14} \text{ cm}^{-3}$  for solar fluences), the diffusion lengths would approach 18  $\mu\text{m}$ . These diffusion lengths, even in the trap-limited regime, rival the best lead iodide perovskites.<sup>46–50</sup> Notwithstanding the toxicity of thallium, this low-bandgap material is therefore fundamentally prone to achieving high solar cell efficiencies even in the presence of a high density of shallow traps if one could fabricate thin films on the order of 300–500 nm, which would absorb the majority of visible solar radiation. Further development of double perovskite band structures to reach properties similar to Ag–Tl with nontoxic substituents should thus be actively pursued.<sup>51</sup> Methods to passivate traps, in particular at the material surface, would dramatically enhance the already-promising functional properties of double perovskites.

Indirect- and symmetry-forbidden bandgap double perovskites appear as promising optoelectronic materials because of their long carrier lifetimes and modest-to-good charge carrier mobilities. Creating materials with symmetry-forbidden bandgaps in the near-infrared, and with an energetically narrow symmetry-forbidden region, such as in Ag–Tl, is a powerful design principle for photovoltaic materials: visible-light absorption coefficients remain high, but carriers quickly relax to the band-edge where recombination is forbidden, leading to long carrier lifetimes.<sup>11</sup> Carrier–defect interactions in the studied double perovskites predominantly involve halide vacancies, which are energetically shallow ( $\sim 80$ – $90 \text{ meV}$ ) and form spontaneously through bromine degassing from the crystal surface. When filled by charges, the resulting neutral defects appear to also contribute to carrier–lattice scattering through the introduction of local structural disorder. Nevertheless, because the trap sites are energetically shallow, they enable defect tolerance through thermal detrapping; carriers thus remain mobile throughout their lifetimes, albeit at substantially reduced mobilities compared to their trap-free mobilities. We demonstrated that despite the large trap densities, particularly near surfaces, the double perovskite crystals studied herein possess large diffusion lengths exceeding 1  $\mu\text{m}$  that rival archetypal lead iodide perovskites. These trap-limited diffusion lengths exceed those necessary for useful charge extraction in optoelectronic devices. Approaches to passivate surfaces to suppress surface-mediated defects would likely enable operating close to a trap-saturated regime at solar

fluences, leading to diffusion lengths exceeding 18  $\mu\text{m}$  and rivaling the very best semiconductors in terms of the ratio of diffusion length to absorption cross section. Finally, we demonstrated the power and importance of spatiotemporally resolving carrier transport over their full lifetimes in defective materials, thus quantifying and decoupling the effects of shallow versus deep trapping versus lattice scattering, as well as near-surface versus bulk contributions to the overall mobility of carriers. Continued systematic studies that disentangle the various contributions to effective carrier mobilities in heterogeneous materials will help design solution-processed, defect-tolerant devices with predictively tuned and beneficial carrier–defect interactions.

## ■ ASSOCIATED CONTENT

### Supporting Information

The Supporting Information is available free of charge at <https://pubs.acs.org/doi/10.1021/acsenerylett.0c00414>.

Materials and methods including safe material handling, material synthesis, data analysis, stroboSCAT setup, and computational details; additional data on Ag–Bi and Ag–Tl carrier dynamics (PDF)

## ■ AUTHOR INFORMATION

### Corresponding Author

**Naomi S. Ginsberg** – Department of Chemistry, Department of Physics, and STROBE, National Science Foundation Science and Technology Center, University of California Berkeley, Berkeley, California, United States; Materials Sciences Division, Lawrence Berkeley National Lab, Berkeley, California, United States; Kavli Energy NanoSciences Institute at Berkeley, Berkeley, California, United States; Molecular Biophysics and Integrated Bioimaging Division, Lawrence Berkeley National Laboratory, Berkeley, California, United States; [orcid.org/0000-0002-5660-3586](https://orcid.org/0000-0002-5660-3586); Email: [nsnginsberg@berkeley.edu](mailto:nsnginsberg@berkeley.edu)

### Authors

**Milan Delor** – Department of Chemistry, University of California Berkeley, Berkeley, California, United States; [orcid.org/0000-0002-9480-9235](https://orcid.org/0000-0002-9480-9235)

**Adam H. Slavney** – Department of Chemistry, Stanford University, Stanford, California, United States

**Nathan R. Wolf** – Department of Chemistry, Stanford University, Stanford, California, United States

**Marina R. Filip** – Department of Physics, University of California Berkeley, Berkeley, California, United States; Molecular Foundry, Lawrence Berkeley National Lab, Berkeley, California, United States

**Jeffrey B. Neaton** – Department of Physics, University of California Berkeley, Berkeley, California, United States; Materials Sciences Division and Molecular Foundry, Lawrence Berkeley National Lab, Berkeley, California, United States; Kavli Energy NanoSciences Institute at Berkeley, Berkeley, California, United States

**Hemamala I. Karunadasa** – Department of Chemistry, Stanford University, Stanford, California, United States; [orcid.org/0000-0003-4949-8068](https://orcid.org/0000-0003-4949-8068)

Complete contact information is available at: <https://pubs.acs.org/doi/10.1021/acsenerylett.0c00414>

### Notes

The authors declare no competing financial interest.

## ■ ACKNOWLEDGMENTS

stroboSCAT measurements and electronic structure calculations were supported by the Center for Computational Study of Excited State Phenomena in Energy Materials (C2SEPEM), which is funded by the U.S. Department of Energy, Office of Science, Basic Energy Sciences, Materials Sciences and Engineering Division under Contract No. DE-AC02-05CH11231, as part of the Computational Materials Sciences Program. stroboSCAT development was supported by STROBE, A National Science Foundation Science & Technology Center under Grant No. DMR 1548924. N.S.G. acknowledges an Alfred P. Sloan Research Fellowship, a David and Lucile Packard Foundation Fellowship for Science and Engineering, and a Camille and Henry Dreyfus Teacher-Scholar Award. Work by A.H.S., N.R.W., and H.I.K. was supported by the Department of Energy, Office of Basic Energy Sciences, Division of Materials Sciences and Engineering, under contract DE-AC02-76SF00515. N.R.W. is supported by a Stanford Interdisciplinary Graduate Fellowship. M.R.F. and J.B.N. acknowledge computational resources at the Molecular Foundry, also supported by the Office of Science, Office of Basic Energy Sciences, of the U.S. DOE under Contract DE-AC02-5CH11231 and resources of the National Energy Research Scientific Computing Center (NERSC).

## ■ REFERENCES

- (1) Nayak, P. K.; Mahesh, S.; Snaith, H. J.; Cahen, D. Photovoltaic Solar Cell Technologies: Analysing the State of the Art. *Nat. Rev. Mater.* **2019**, *4*, 269–285.
- (2) Ball, J. M.; Petrozza, A. Defects in Perovskite-Halides and Their Effects in Solar Cells. *Nat. Energy* **2016**, *1*, 16149.
- (3) Li, W.; Wang, Z.; Deschler, F.; Gao, S.; Friend, R. H.; Cheetham, A. K. Chemically Diverse and Multifunctional Hybrid Organic-Inorganic Perovskites. *Nat. Rev. Mater.* **2017**, *2*, 16099.
- (4) Giustino, F.; Snaith, H. J. Toward Lead-Free Perovskite Solar Cells. *ACS Energy Lett.* **2016**, *1*, 1233–1240.
- (5) Maughan, A. E.; Ganose, A. M.; Scanlon, D. O.; Neilson, J. R. Perspectives and Design Principles of Vacancy-Ordered Double Perovskite Halide Semiconductors. *Chem. Mater.* **2019**, *31*, 1184–1195.
- (6) McClure, E. T.; Ball, M. R.; Windl, W.; Woodward, P. M. Cs<sub>2</sub>AgBiX<sub>6</sub> (X = Br, Cl): New Visible Light Absorbing, Lead-Free Halide Perovskite Semiconductors. *Chem. Mater.* **2016**, *28*, 1348–1354.
- (7) Pan, W.; Wu, H.; Luo, J.; Deng, Z.; Ge, C.; Chen, C.; Jiang, X.; Yin, W.-J.; Niu, G.; Zhu, L.; Yin, L.; Zhou, Y.; Xie, Q.; Ke, X.; Sui, M.; Tang, J. Cs<sub>2</sub>AgBiBr<sub>6</sub> Single-Crystal X-Ray Detectors with a Low Detection Limit. *Nat. Photonics* **2017**, *11*, 726–732.
- (8) Liang, L.; Gao, P. Lead-Free Hybrid Perovskite Absorbers for Viable Application: Can We Eat the Cake and Have It Too? *Adv. Sci.* **2018**, *5*, 1700331.
- (9) Lyu, M.; Yun, J.-H.; Chen, P.; Hao, M.; Wang, L. Addressing Toxicity of Lead: Progress and Applications of Low-Toxic Metal Halide Perovskites and Their Derivatives. *Adv. Energy Mater.* **2017**, *7*, 1602512.
- (10) Slavney, A. H.; Hu, T.; Lindenberg, A. M.; Karunadasa, H. I. A Bismuth-Halide Double Perovskite with Long Carrier Recombination Lifetime for Photovoltaic Applications. *J. Am. Chem. Soc.* **2016**, *138*, 2138–2141.
- (11) Slavney, A. H.; Leppert, L.; Saldívar Valdes, A.; Bartesaghi, D.; Savenije, T. J.; Neaton, J. B.; Karunadasa, H. I. Small-Band-Gap Halide Double Perovskites. *Angew. Chem., Int. Ed.* **2018**, *57*, 12765–12770.
- (12) Hoye, R. L. Z.; Eyre, L.; Wei, F.; Brivio, F.; Sadhanala, A.; Sun, S.; Li, W.; Zhang, K. H. L.; MacManus-Driscoll, J. L.; Bristowe, P. D.; Friend, R. H.; Cheetham, A. K.; Deschler, F. Fundamental Carrier

Lifetime Exceeding 1 Ms in Cs<sub>2</sub>AgBiBr<sub>6</sub> Double Perovskite. *Adv. Mater. Interfaces* **2018**, *5*, 1800464.

(13) Steele, J. A.; Pan, W.; Martin, C.; Keshavarz, M.; Debroye, E.; Yuan, H.; Banerjee, S.; Fron, E.; Jonckheere, D.; Kim, C. W.; Baekelant, W.; Niu, G.; Tang, J.; Vanacken, J.; Van der Auweraer, M.; Hofkens, J.; Roeffaers, M. B. J. Photophysical Pathways in Highly Sensitive Cs<sub>2</sub>AgBiBr<sub>6</sub> Double-Perovskite Single-Crystal X-Ray Detectors. *Adv. Mater.* **2018**, *30*, 1870353.

(14) Kapil, G.; Ohta, T.; Koyanagi, T.; Vigneshwaran, M.; Zhang, Y.; Ogomi, Y.; Pandey, S. S.; Yoshino, K.; Shen, Q.; Toyoda, T.; Rahman, M. M.; Minemoto, T.; Murakami, T. N.; Segawa, H.; Hayase, S. Investigation of Interfacial Charge Transfer in Solution Processed Cs<sub>2</sub>SnI<sub>6</sub> Thin Films. *J. Phys. Chem. C* **2017**, *121*, 13092–13100.

(15) Volonakis, G.; Filip, M. R.; Haghighirad, A. A.; Sakai, N.; Wenger, B.; Snaith, H. J.; Giustino, F. Lead-Free Halide Double Perovskites via Heterovalent Substitution of Noble Metals. *J. Phys. Chem. Lett.* **2016**, *7*, 1254–1259.

(16) Laporte, O.; Meggers, W. F. Some Rules of Spectral Structure. *J. Opt. Soc. Am.* **1925**, *11*, 459–463.

(17) Meng, W.; Wang, X.; Xiao, Z.; Wang, J.; Mitzi, D. B.; Yan, Y. Parity-Forbidden Transitions and Their Impact on the Optical Absorption Properties of Lead-Free Metal Halide Perovskites and Double Perovskites. *J. Phys. Chem. Lett.* **2017**, *8*, 2999–3007.

(18) Bartesaghi, D.; Slavney, A. H.; Gélvez-Rueda, M. C.; Connor, B. A.; Grozema, F. C.; Karunadasa, H. I.; Savenije, T. J. Charge Carrier Dynamics in Cs<sub>2</sub>AgBiBr<sub>6</sub> Double Perovskite. *J. Phys. Chem. C* **2018**, *122*, 4809–4816.

(19) Hutter, E. M.; Gélvez-Rueda, M. C.; Bartesaghi, D.; Grozema, F. C.; Savenije, T. J. Band-Like Charge Transport in Cs<sub>2</sub>AgBiBr<sub>6</sub> and Mixed Antimony-Bismuth Cs<sub>2</sub>AgBi<sub>1-x</sub>Sb<sub>x</sub>Br<sub>6</sub> Halide Double Perovskites. *ACS Omega* **2018**, *3*, 11655–11662.

(20) Schulz, P.; Cahen, D.; Kahn, A. Halide Perovskites: Is It All about the Interfaces? *Chem. Rev.* **2019**, *119*, 3349–3417.

(21) Delor, M.; Weaver, H. L.; Yu, Q.; Ginsberg, N. S. Imaging Material Functionality through Three-Dimensional Nanoscale Tracking of Energy Flow. *Nat. Mater.* **2020**, *19*, 56–62.

(22) Ginsberg, N. S.; Tisdale, W. A. Spatially Resolved Exciton and Charge Transport in Emerging Semiconductors. *Annu. Rev. Phys. Chem.* **2020**, *71*. DOI: 10.1146/annurev-physchem-052516-050703

(23) Zhu, T.; Snaider, J. M.; Yuan, L.; Huang, L. Ultrafast Dynamic Microscopy of Carrier and Exciton Transport. *Annu. Rev. Phys. Chem.* **2019**, *70*, 219–244.

(24) Gabriel, M. M.; Kirschbrown, J. R.; Christesen, J. D.; Pinion, C. W.; Zigler, D. F.; Grumstrup, E. M.; Mehl, B. P.; Cating, E. E. M.; Cahoon, J. F.; Papanikolas, J. M. Direct Imaging of Free Carrier and Trap Carrier Motion in Silicon Nanowires by Spatially-Separated Femtosecond Pump-Probe Microscopy. *Nano Lett.* **2013**, *13*, 1336–1340.

(25) Guo, Z.; Manser, J. S.; Wan, Y.; Kamat, P. V.; Huang, L. Spatial and Temporal Imaging of Long-Range Charge Transport in Perovskite Thin Films by Ultrafast Microscopy. *Nat. Commun.* **2015**, *6*, 7471–7479.

(26) Hill, A. H.; Smyser, K. E.; Kennedy, C. L.; Massaro, E. S.; Grumstrup, E. M. Screened Charge Carrier Transport in Methylammonium Lead Iodide Perovskite Thin Films. *J. Phys. Chem. Lett.* **2017**, *8*, 948–953.

(27) Akselrod, G. M.; Deotare, P. B.; Thompson, N. J.; Lee, J.; Tisdale, W. a.; Baldo, M. a.; Menon, V. M.; Bulović, V. Visualization of Exciton Transport in Ordered and Disordered Molecular Solids. *Nat. Commun.* **2014**, *5*, 3646.

(28) Kulig, M.; Zipfel, J.; Nagler, P.; Blanter, S.; Schüller, C.; Korn, T.; Paradiso, N.; Glazov, M. M.; Chernikov, A. Exciton Diffusion and Halo Effects in Atomically Thin Semiconductors. *Phys. Rev. Lett.* **2018**, *120*, 207401.

(29) Block, A.; Liebel, M.; Yu, R.; Spector, M.; Sivan, Y.; García de Abajo, F. J.; van Hulst, N. F. Tracking Ultrafast Hot-Electron Diffusion in Space and Time by Ultrafast Thermomodulation Microscopy. *Sci. Adv.* **2019**, *5*, No. eaav8965.

(30) Schnedermann, C.; Sung, J.; Pandya, R.; Verma, S. D.; Chen, R. Y. S.; Gauriot, N.; Bretscher, H. M.; Kukura, P.; Rao, A. Ultrafast Tracking of Exciton and Charge Carrier Transport in Optoelectronic Materials on the Nanometer Scale. *J. Phys. Chem. Lett.* **2019**, *10*, 6727–6733.

(31) deQuilettes, D. W.; Jariwala, S.; Burke, S.; Ziffer, M. E.; Wang, J. T.-W.; Snaith, H. J.; Ginger, D. S. Tracking Photoexcited Carriers in Hybrid Perovskite Semiconductors: Trap-Dominated Spatial Heterogeneity and Diffusion. *ACS Nano* **2017**, *11*, 11488–11496.

(32) Kentsch, R.; Scholz, M.; Horn, J.; Schlettwein, D.; Oum, K.; Lenzer, T. Exciton Dynamics and Electron–Phonon Coupling Affect the Photovoltaic Performance of the Cs<sub>2</sub>AgBiBr<sub>6</sub> Double Perovskite. *J. Phys. Chem. C* **2018**, *122*, 25940–25947.

(33) Folie, B. D.; Tan, J. A.; Huang, J.; Sercel, P. C.; Delor, M.; Lai, M.; Lyons, J. L.; Bernstein, N.; Efros, A. L.; Yang, P.; Ginsberg, N. S. Effect of Anisotropic Confinement on Electronic Structure and Dynamics of Band Edge Excitons in Inorganic Perovskite Nanowires. *J. Phys. Chem. A* **2020**, *124*, 1867–1876.

(34) Murali, B.; Dey, S.; Abdelhady, A. L.; Peng, W.; Alarousu, E.; Kirmani, A. R.; Cho, N.; Sarmah, S. P.; Parida, M. R.; Saidaminov, M. I.; Zhumekenov, A. A.; Sun, J.; Alias, M. S.; Yengel, E.; Ooi, B. S.; Amassian, A.; Bakr, O. M.; Mohammed, O. F. Surface Restructuring of Hybrid Perovskite Crystals. *ACS Energy Lett.* **2016**, *1*, 1119–1126.

(35) Chattopadhyay, D.; Queisser, H. J. Electron Scattering by Ionized Impurities in Semiconductors. *Rev. Mod. Phys.* **1981**, *53*, 745–768.

(36) Xiao, Z.; Meng, W.; Wang, J.; Yan, Y. Thermodynamic Stability and Defect Chemistry of Bismuth-Based Lead-Free Double Perovskites. *ChemSusChem* **2016**, *9*, 2628–2633.

(37) Yin, W.-J.; Shi, T.; Yan, Y. Unusual Defect Physics in CH<sub>3</sub>NH<sub>3</sub>PbI<sub>3</sub> Perovskite Solar Cell Absorber. *Appl. Phys. Lett.* **2014**, *104*, No. 063903.

(38) Buin, A.; Pietsch, P.; Xu, J.; Voznyy, O.; Ip, A. H.; Comin, R.; Sargent, E. H. Materials Processing Routes to Trap-Free Halide Perovskites. *Nano Lett.* **2014**, *14*, 6281–6286.

(39) Jin, H.; Debroye, E.; Keshavarz, M.; Scheblykin, I. G.; Roeffaers, M. B. J.; Hofkens, J.; Steele, J. A. It's a Trap! On the Nature of Localised States and Charge Trapping in Lead Halide Perovskites. *Mater. Horiz.* **2020**, *7*, 397.

(40) Kang, J.; Wang, L.-W. High Defect Tolerance in Lead Halide Perovskite CsPbBr<sub>3</sub>. *J. Phys. Chem. Lett.* **2017**, *8*, 489–493.

(41) Li, C.; Duan, L.; Li, H.; Qiu, Y. Universal Trap Effect in Carrier Transport of Disordered Organic Semiconductors: Transition from Shallow Trapping to Deep Trapping. *J. Phys. Chem. C* **2014**, *118*, 10651–10660.

(42) Vladimirov, I.; Kühn, M.; Geßner, T.; May, F.; Weitz, R. T. Energy Barriers at Grain Boundaries Dominate Charge Carrier Transport in an Electron-Conductive Organic Semiconductor. *Sci. Rep.* **2018**, *8*, 14868.

(43) Zelewski, S. J.; Urban, J. M.; Surrente, A.; Maude, D. K.; Kuc, A.; Schade, L.; Johnson, R. D.; Dollmann, M.; Nayak, P. K.; Snaith, H. J.; Radaelli, P.; Kudrawiec, R.; Nicholas, R. J.; Plochocka, P.; Baranowski, M. Revealing the Nature of Photoluminescence Emission in the Metal-Halide Double Perovskite Cs<sub>2</sub>AgBiBr<sub>6</sub>. *J. Mater. Chem. C* **2019**, *7*, 8350–8356.

(44) Johnston, M. B.; Herz, L. M. Hybrid Perovskites for Photovoltaics: Charge-Carrier Recombination, Diffusion, and Radiative Efficiencies. *Acc. Chem. Res.* **2016**, *49*, 146–154.

(45) Karakus, M.; Jensen, S. A.; D'Angelo, F.; Turchinovich, D.; Bonn, M.; Cánovas, E. Phonon-Electron Scattering Limits Free Charge Mobility in Methylammonium Lead Iodide Perovskites. *J. Phys. Chem. Lett.* **2015**, *6*, 4991–4996.

(46) Shi, D.; Adinolfi, V.; Comin, R.; Yuan, M.; Alarousu, E.; Buin, A.; Chen, Y.; Hoogland, S.; Rothenberger, A.; Katsiev, K.; Losovyj, Y.; Zhang, X.; Dowben, P. A.; Mohammed, O. F.; Sargent, E. H.; Bakr, O. M. Low Trap-State Density and Long Carrier Diffusion in Organolead Trihalide Perovskite Single Crystals. *Science* **2015**, *347*, 519–522.

(47) Stranks, S. D.; Eperon, G. E.; Grancini, G.; Menelaou, C.; Alcocer, M. J. P.; Leijtens, T.; Herz, L. M.; Petrozza, A.; Snaith, H. J.

Electron-Hole Diffusion Lengths Exceeding 1 Micrometer in an Organometal Trihalide Perovskite Absorber. *Science* **2013**, *342*, 341–344.

(48) Xing, G.; Mathews, N.; Sun, S.; Lim, S. S.; Lam, Y. M.; Gratzel, M.; Mhaisalkar, S.; Sum, T. C. Long-Range Balanced Electron and Hole-Transport Lengths in Organic-Inorganic CH<sub>3</sub>NH<sub>3</sub>PbI<sub>3</sub>. *Science* **2013**, *342*, 344–347.

(49) Elbaz, G. A.; Straus, D. B.; Semonin, O. E.; Hull, T. D.; Paley, D. W.; Kim, P.; Owen, J. S.; Kagan, C. R.; Roy, X. Unbalanced Hole and Electron Diffusion in Lead Bromide Perovskites. *Nano Lett.* **2017**, *17*, 1727–1732.

(50) Reid, O. G.; Yang, M.; Kopidakis, N.; Zhu, K.; Rumbles, G. Grain-Size-Limited Mobility in Methylammonium Lead Iodide Perovskite Thin Films. *ACS Energy Lett.* **2016**, *1*, 561–565.

(51) Lindquist, K. P.; Mack, S. A.; Slavney, A. H.; Leppert, L.; Gold-Parker, A.; Stebbins, J. F.; Salleo, A.; Toney, M. F.; Neaton, J. B.; Karunadasa, H. I. Tuning the Bandgap of Cs<sub>2</sub>AgBiBr<sub>6</sub> through Dilute Tin Alloying. *Chem. Sci.* **2019**, *10*, 10620–10628.